Sensors & Actuators: B. Chemical 304 (2020) 127287

Contents lists available at ScienceDirect

Sensors and Actuators B: Chemical

journal homepage: www.elsevier.com/locate/snb

Visible light activated excellent NO_2 sensing based on 2D/2D ZnO/g-C_3N_4 heterojunction composites

Hongtao Wang, Jihao Bai, Meng Dai, Kunpeng Liu, Yueying Liu, Linsheng Zhou, Fengmin Liu*, Fangmeng Liu, Yuan Gao, Xu Yan, Lu Geyu*

State Key Laboratory on Integrated Optoelectronics, College of Electronic Science and Engineering, Jilin University, 2699 Qianjin Street, Changchun 130012, China

ARTICLE INFO

Keywords:
NO_2 gas sensor
ZnO
g-C_3N_4
Room temperature
Visible light
Interface

ABSTRACT

In this work, 2D/2D ZnO/g-C_3N_4 heterojunction composite was synthesized through an ultrasonic mixing and subsequent calcination process. The gas-sensing performance to NO_2 was investigated at room temperature activated by visible/ultra-violet LED light sources. Noticeably, when ZnO/g-C_3N_4 composite is illuminated by 460 nm light, it exhibits the highest response of 44.8 to 7 ppm NO_2, and the response and recovery time is 142 and 190 s, respectively. Furthermore, it possesses excellent repeatability and selectivity to NO_2, and the limit of detection is 38 ppb. In addition, the effect of humidity on the sensing performance under visible light was also investigated. The excellent gas-sensing performance is attributed to the absorbance of g-C_3N_4 in the visible light region and the charge separation at the interface between ZnO and g-C_3N_4.

1. Introduction

To improve the sensing performance of gas sensors based on metal oxide semiconductor (MOS), researchers have developed many modification approaches such as regulating the size and morphology of sensing material [1,2], doping metal ion [3,4], or constructing heterostructure [5–7]. As a result, the sensitivity, selectivity, and the response and recovery speed of gas sensors are greatly improved. However, these sensors usually need to be heated to a few hundred degrees to provide sufficient energy for the adsorption of test gases and the redox reaction with the negative oxygen species, which consumes amounts of extra energy and leads to a decrease in stability [8,9]. In addition, it is also not conducive to the development of flexible and wearable sensor devices [10,11].

Light excitation instead of heating method also can increase the carrier concentration in semiconductors and activate the sensing reaction with test gases. Furthermore, the highly active photogenerated electron-hole pairs can not only improve the gas-sensing response, but also reduce the response and recovery time [12,13]. Therefore, light excitation is an effective approach to realize the detection of harmful gases at room temperature for gas sensors based on MOS. UV-activated gas sensors have been widely studied and achieved good results [14–16]. However, the strong photon energy of UV light can damage human skin or eyes, which seriously hinders the practical application of sensor devices. To broaden the wavelength of excitation sources and reduce the harm caused by UV light, researchers have made much related research such as selecting narrow bandgap semiconductors as sensing material or using the surface plasma resonance effect of precious metal. For example, Lee et al. prepared CdS nanocrystals by chemical deposition method and studied the NO_2 sensing performance activated by green LED light source [17]. Chizhov et al. sensitized ZnO with CdSe quantum dots, which greatly improved the visible light absorption of ZnO and realized the room-temperature detection of NO_2 [18]. Zhang et al. extended the absorption of ZnO to blue light region by loading Ag nanoparticles and achieved excellent sensing performance to NO_2 under 470 nm light [19]. However, sensitizers based on Cd are unstable and poisonous, and the loading process of precious metal is prone to happen agglomeration. Therefore, it is very meaningful to develop new photosensitizers for gas sensors activated by visible light.

Graphitic carbon nitride (g-C_3N_4) is a conjugated organic semiconductor consisted of sp^2 hybridized nitrogen and carbon atoms [20–22]. Due to its low-cost synthesis process and unique layer structure, researchers gradually pay attention to its application in various fields such as dye degradation [23], water splitting [24] and gas sensors [25] in recent years. The excellent catalytic activity in the visible light region is the most important property for g-C_3N_4 due to its narrow bandgap [26–28]. Besides, g-C_3N_4 is much safer and more suitable for sensor applications compared with other photosensitizers. To date, g-C_3N_4 as a photosensitizer applied for gas sensors activated by visible

* Corresponding authors.
E-mail addresses: liufm@jlu.edu.cn (F. Liu), lugy@jlu.edu.cn (L. Geyu).

https://doi.org/10.1016/j.snb.2019.127287
Received 1 August 2019; Received in revised form 9 October 2019; Accepted 14 October 2019
Available online 19 October 2019
0925-4005/

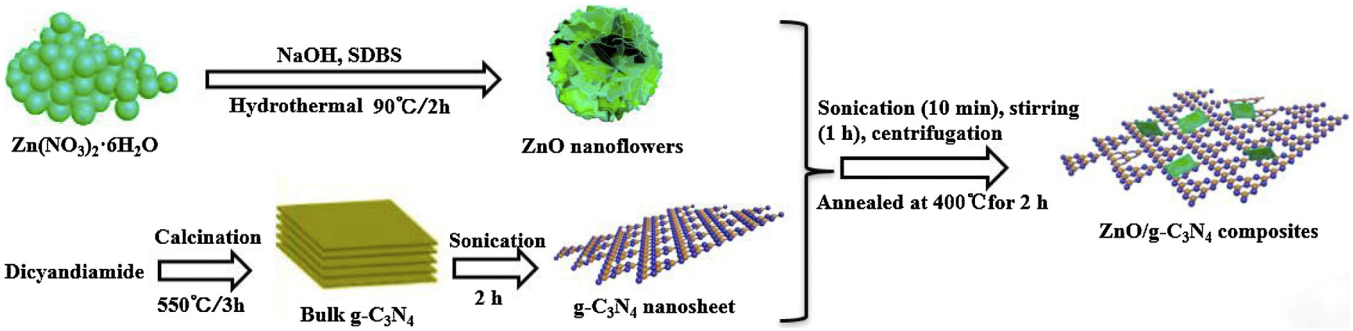

Fig. 1. The diagram of synthesis process of ZnO/g-C_3N_4 composites.

light has not been reported. Therefore, we chose g-C_3N_4 as the photosensitizer in this work.

Among various MOS, ZnO is a typical n-type semiconductor sensing material with high electron mobility [29], controllable microstructures [30], good thermal and chemical stability [31], and appropriate bandgap (3.2 eV), which is widely applied in NO_2 sensors activated by light [32]. Furthermore, the combination of ZnO and g-C_3N_4 has been widely used in the field of photocatalysis [33,34] and the results show that the catalytic performance was largely improved in the visible light region. TiO_2 is also often used in photocatalysis [35], but it has the problem of high resistance, which is not suitable for sensor application. With regard to other MOS such as SnO_2, In_2O_3, and WO_3, their photosensitivity is not as good as ZnO [36]. Therefore, in this work, the research focuses on the feasibility of using g-C_3N_4 as photosensitizer to modify ZnO to detect NO_2 at room temperature activated by visible light.

In this paper, ZnO/g-C_3N_4 composites were successfully synthesized via ultrasonic mixing and subsequent calcination process. The gas-sensing performance to NO_2 was systematically investigated at room temperature, and the results show that no matter under UV (365 nm) or visible (410 nm, 420 nm, 460 nm) light excitation, the 10 wt% g-C_3N_4 loaded ZnO exhibits much higher response than other samples. When under 460 nm light excitation, its response reaches the maximum. Then we conducted the cycle and selectivity tests, and the results show that the ZnO/g-C_3N_4 composite has excellent selectivity, stability, and sensitivity to NO_2. The effect of humidity on the sensing characteristics was also studied. This work not only provides an excellent sensing material for NO_2 gas sensors activated by visible light, but also elucidates the sensing mechanism under visible light excitation.

2. Experimental section

2.1. Synthesis of pure ZnO nanoflower

All reagents – zinc nitrate hexahydrate ($Zn(NO_3)_2{\cdot}6H_2O$), sodium hydroxide (NaOH), sodium dodecyl benzene sulfonate (SDBS), dicyandiamide – were purchased from Aladdin Reagent Co., Ltd. (Shanghai, China), and were of analytic grade and used as received without further purification. In material synthesis process, deionized water was used to prepare all the aqueous solution. The pure ZnO nanoflowers assembled of nanosheets were prepared via a facile hydrothermal method as follows. 5.94 g of $Zn(NO_3)_2{\cdot}6H_2O$ was dissolved in 20 ml of deionized water. 2.4 g of NaOH and 174 mg of SDBS were mixed in 35 ml of deionized water. Then, mixing the two solution under vigorous stirring and remaining stirring for another 30 min. at room temperature. The mixing solution was then transferred into a 100 ml of autoclave and placed in an oven at 90 °C for 2 h. The white product deposited on the bottom were collected, washed with water and ethanol for three times and dried in an oven at 60 °C for 6 h. Finally, the white powder was calcined in a muffle oven at 400 °C for 2 h with a ramp rate of 10 °C min^{-1}.

2.2. Synthesis of g-C_3N_4

Bulk g-C_3N_4 was prepared by heating dicyandiamide from the room temperature to 550 °C with a ramp rate of 2 °C min^{-1} in static air, and then the temperature was kept at 550 °C for 3 h.

2.3. Synthesis of ZnO/g-C_3N_4 composites

g-C_3N_4 was synthesized through calcining dicyandiamide at 550℃, and ZnO was prepared by a facile hydrothermal method. Therefore, we have tried three approaches to prepare the ZnO/g-C_3N_4 composites. The first approach was to add as-prepared g-C_3N_4 to the precursor solution of ZnO. The second approach was to add as-prepared ZnO to dicyandiamide. The third approach was mixing as-prepared ZnO and g-C_3N_4 through ultrasonic processing, and then calcining the mixture to form ZnO/g-C_3N_4 composites. The first and second approaches were not ideal in terms of morphology and gas-sensing response, so we chose the third approach. The detailed steps are as follows. A certain quantity of the obtained bulk g-C_3N_4 was dispersed in 30 ml of deionized water and followed by ultrasonic treatment for 2 h. 100 mg of ZnO nanoflowers without calcination was added to the above suspension and mixed under ultrasound. Then the suspension was stirred for another 1 h, centrifuged with ethanol and dried in an oven at 60 °C for 6 h. Finally, the obtained buff powder was calcined in a muffle oven at 400 °C for 2 h with a ramp rate of 10 °C min^{-1}. In this work, we added 5, 10, and 15 mg g-C_3N_4 into 100 mg ZnO, and labeled them ZnO/g-C_3N_4-5 wt%, ZnO/g-C_3N_4-10 wt%, ZnO/g-C_3N_4-15 wt%, respectively. The synthesis process of ZnO/g-C_3N_4 composites was shown in Fig. 1.

2.3.1. Sample characterization

The surface morphologies of as-prepared samples were characterized by a field emission scanning electron microscope (FESEM, JEOL JSM-7500 F, operated at an accelerating voltage of 15 kV) attached with energy dispersive spectroscopy (EDS). The crystal structures of samples were analyzed by a powder X-ray diffractometer (XRD: Rigaku D/Max-2550 VX-ray diffractometer) equipped with Cu Kα radiation (λ = 1.5418 Å and 2θ = 20–80°). Fourier transform infrared spectra (FT-IR) were recorded on a Nicolet iS50 FT-IR spectrometer (Thermo Fisher Scientific, USA) in the frequency range of 700–3500 cm^{-1} with a resolution of 0.4 cm^{-1}. Ultraviolet-visible (UV–vis) diffuse reflectance spectra were measured by a UV–vis spectrophotometer (Shimadzu UV2550, Japan). The X-ray photoelectron spectroscopy (XPS) measurements were performed in a VG ESCALAB 210 (VG Scientific, UK) photoelectron spectrometer equipped with a Mg $K\alpha_{1,2}$ exciting source and source power of 300 W. All the binding energies of the elements were calibrated to the carbon binding energy of 284.8 eV. The Brunauer-Emmett-Teller (BET) specific surface area of samples were investigated by measuring nitrogen adsorption-desorption isotherm with a Physisorption Analyzer (Micromeritics Instrument Corporation TriStar II 3020).

2.3.2. The fabrication and measurement of gas sensors

The fabrication process of gas sensors was referred in our previous reports [37,38] and as follows. A certain amount of as-prepared sample was mixed with ethanol to form a slurry. Then the slurry was coated onto the outside surface of an alumina ceramic tube using a small brush. The four corners of the ceramic tube have gold electrodes for signal output, and then the ceramic tube was calcined at 300 °C for 2 h to sinter the sensing layer. Finally, the ceramic tube was welded to a six-legged base and aged for three days before conducting sensing tests. The LED was installed on the top of the base to activate the sensor device. The light intensity was measured by a light irradiation meter (UV-313/340, Zhuhai Tianchuang Instrument Company, China). Besides, all the LED light sources used in the test were purchased from LG Electronics Company (Korea). The applied voltage of light sources is 3.5 V, and the power is 3 W.

Sensing tests were carried out in a static test system. Two gas chambers whose volume is 1 L were used during the sensing test, and a certain concentration of NO_2 is pre-injected into one of the gas chambers through a microsyringe while the other gas chamber contains pure air. When the resistance stabilizes in air, the sensor element was moved quickly to the gas chamber containing NO_2. It is important to note that there is almost no change in atmosphere of the gas chambers during the movement. If both gas chambers contain pure air, there will be no change in resistance. The whole test process was carried out at room temperature, and the relative humidity (RH) indoor was maintained at 25%. The resistance of sensors was measured by a multimeter (Fluke 8846A) and recorded in real time by a data-acquisition PC. The gas-sensing response is defined as $S = R_g/R_a$, where R_g and R_a are the real-time resistance of the sensor after exposing to NO_2 gas and the baseline resistance in pure air. In addition, the response and recovery time is defined as the time taken by the sensor to achieve 90% of the total resistance change. The diagram of gas-sensing test system was shown in Fig. S1b.

3. Results and discussion

3.1. Characterization

The morphology of as-prepared samples was characterized by SEM. As shown in Fig. 2(a and b), pure ZnO exhibits a flower-like structure, which is 800–900 nm in diameter and composed of flaky petals with thickness ranging from 70 to 90 nm. The obtained g-C_3N_4 in Fig. 2c presents sheet-structure with uneven shape on scale of tens of microns, which can provide huge contact surface with ZnO and large light absorption area. With regard to ZnO/g-C_3N_4 composite, it exhibits a morphology that ZnO nanosheets are distributed on the surface of g-C_3N_4, as shown in Fig. 2(d and e). The element distribution and EDS analysis of ZnO/g-C_3N_4-10 wt% were shown in Fig. S2. Well defined peaks corresponding to Zn, O, C and N can be clearly seen in the spectra. Except for Zn, O, C and N, no other peak related to any other elemental impurity confirms that ZnO/g-C_3N_4-10 wt% are of high purity. According to the EDS test results, the mass percentage of g-C_3N_4 to ZnO is about 0.048: 1.

The crystal phase of as-prepared samples was confirmed by XRD measurements, as shown in Fig. 2f. The peak appearing in g-C_3N_4 at 27.4° is indexed to (002) diffraction plane of the graphite-like carbon nitride and corresponding to the inter-layer structural packing [39]. Pure ZnO exhibits eleven diffraction peaks, which match well with those of the hexagonal wurtzite ZnO (JCPDS File No. 89–511). The characteristic peak of g-C_3N_4 is not observed in the XRD spectra of ZnO/g-C_3N_4 composites, which is possibly due to that g-C_3N_4 is covered by ZnO nanosheets and difficult to probe.

Fig. 3 shows the FT-IR spectra of pure ZnO, g-C_3N_4 and ZnO/g-C_3N_4 composites. In the spectrum of g-C_3N_4, the band near 808 cm^{-1} is indicative of the s-triazine ring vibrations, and the absorption band near 1640 cm^{-1} is attributed to the C—N stretching [40]. The four band near at 1240, 1320, 1403, and 1557 cm^{-1} is attributed to the aromatic C—N stretching while the broad band near 3160 cm^{-1} is corresponded to the stretching pattern of NH_2 or NH groups at the defect sites of the end of aromatic ring [41]. All the characteristic absorption band of g-C_3N_4 except the band at 3160 cm^{-1} appears in the spectra of ZnO/g-C_3N_4 composites, which indicates that ZnO and the g-C_3N_4 are co-existing.

To investigate the absorbance of ZnO after modification, UV–vis measurements were conducted, and the spectra were shown in Fig. 4. It can be seen that pure ZnO exhibits a sharp absorption band edge at 380 nm, which is caused by its wide bandgap. In contrast, ZnO/g-C_3N_4 composites can absorb the visible light ranging from 400 to 500 nm, and the absorption intensity of visible light increases as the g-C_3N_4 amount increases. Therefore, we chose 365, 410, 420, and 460 nm LED as the light excitation sources in the gas-sensing tests.

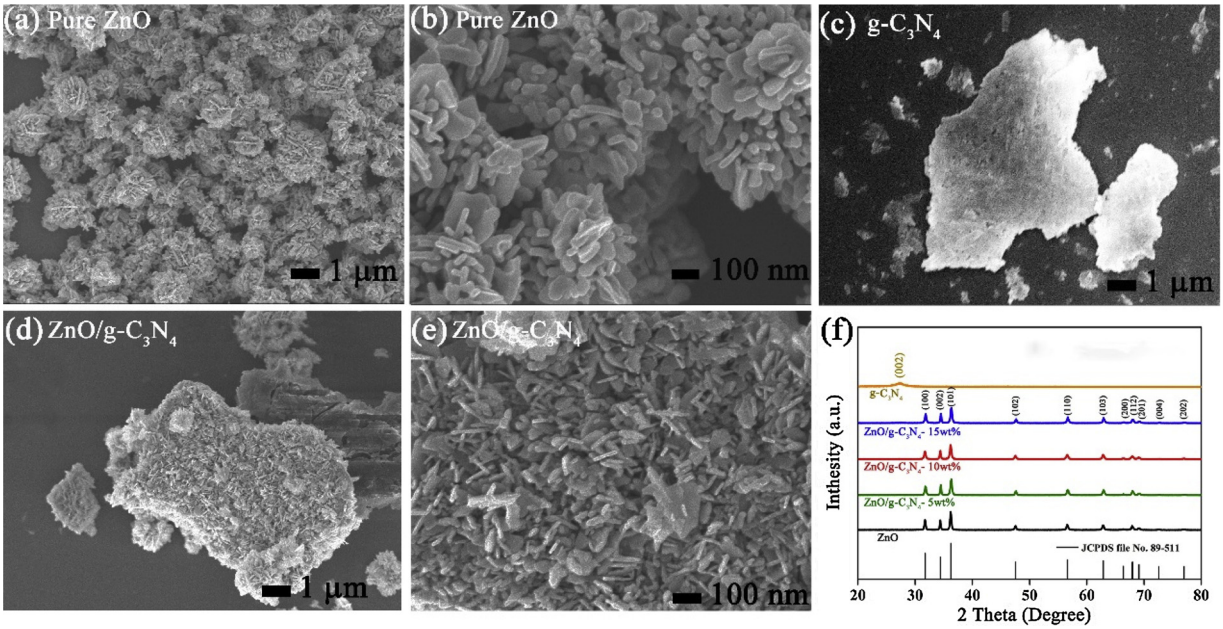

Fig. 2. The SEM images of (a) pure ZnO nanoflowers (low-resolution); (b) pure ZnO nanoflowers (high-resolution); (c) g-C_3N_4; (d) ZnO/g-C_3N_4 composite (low-resolution); (e) ZnO/g-C_3N_4 composite (high-resolution); (f) XRD patterns of pure ZnO, g-C_3N_4 and the ZnO/g-C_3N_4 composites.

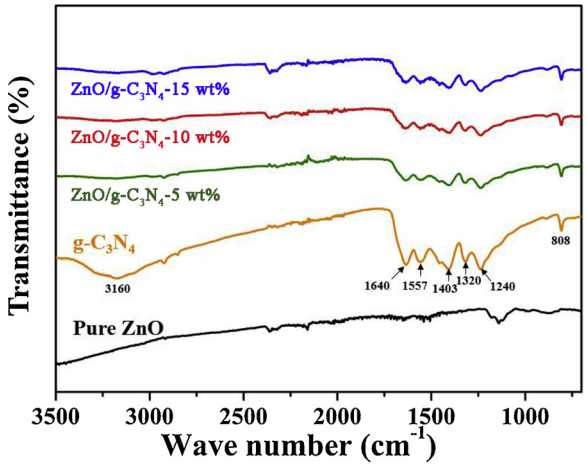

Fig. 3. FT-IR spectra of pure ZnO, g-C_3N_4 and ZnO/g-C_3N_4 composites.

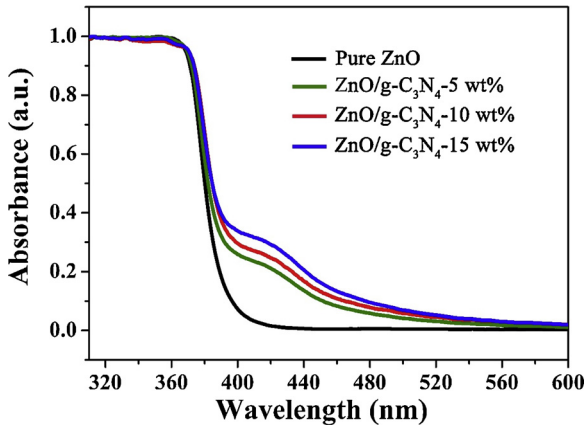

Fig. 4. UV–vis spectra of pure ZnO and ZnO/g-C_3N_4 composites.

The surface elemental composition and chemical states of ZnO/g-C_3N_4 composites were studied by XPS measurements, here ZnO/g-C_3N_4-10 wt% was chosen to illustrate as an example. As shown in Fig. 5a, the Zn 2p spectrum shows two main peaks located at approximately 1020.8 and 1043.9 eV, which indicates the electronic states of Zn $2p_{3/2}$ and Zn $2p_{1/2}$, respectively [42]. The C 1s spectrum in Fig. 5b exhibits three peaks at the binding energies of 284.6, 286.0, and 288.3 eV, which are attributed to C—C, C—NH_2, and C═N, respectively. The N 1s is divided to three distinct peaks located at about 398.3, 400.3, and 404.8 eV, respectively. The peak at 398.7 eV is due to the C═N—C. The peaks centered at 400.2 and 404.8 eV can be assigned to the charge effect and the N-$(C)_3$, respectively [43]. The O 1s spectrum in Fig. 5d can be described to two peaks located at 529.8 and 531.2 eV, which are related to the lattice oxygen in Zn–O lattice framework and the surface chemical adsorption of oxygen, respectively [44,45]. As shown in Table 1, it can be roughly estimated the atomic percentage of N to Zn in ZnO/g-C_3N_4-10 wt% is 0.09: 1, that is the mass percentage of g-C_3N_4 to ZnO is 0.02:1, according to the XPS test results. In this work, ZnO are mainly distributed on the surface of g-C_3N_4, and XPS analyzes the surface chemical composition of materials and cannot reflect the bulk chemical composition. Therefore, the XPS showed a lower mass percentage of g-C_3N_4 to ZnO than that of in the reactants. It is worth mentioning that the difference in mass percentage measured by EDS and XPS is caused by different sounding depth. Generally speaking, XPS has a sounding depth of several nanometers while EDS can reach micron. As shown in SEM images, ZnO are mainly distributed on the surface of g-C_3N_4. As a result, the mass percentage of g-C_3N_4 to ZnO measured by EDS is larger than that of XPS.

The N_2 adsorption/desorption isotherms of as-prepared samples were shown in Fig. S3. Pure ZnO and ZnO/g-C_3N_4 composites all show typical type IV adsorption isotherms with a H_3-type hysteresis loop, indicating the presence of the mesoporous structure. A summary of the BET specific surface area, pore volume, and the pore size was shown in Table 2. It can be seen that the specific surface area has no much change between pure ZnO and ZnO/g-C_3N_4 composites.

3.2. Gas-sensing properties of ZnO/g-C_3N_4 composites

In the gas-sensing tests, our samples were coated on ceramic tubes to fabricate gas sensors for investigating their sensing performance at room temperature (27 °C, 25% RH). The sensing performance of samples in dark condition was not investigated due to the high resistance, which is beyond the measuring range of multimeter (Fluke 8846A). Firstly, the sensing performance of as-prepared samples activated by LED light sources with different wavelength were investigated, and the responses were shown in Fig. 6. It can be seen that ZnO/g-C_3N_4-10 wt% exhibits the highest response to 7 ppm NO_2 when it is activated by 460 nm light. For all ZnO/g-C_3N_4 composites, the response to NO_2 increase with the increase of wavelength, which is related to the absorbance characteristics of the photosensitizer and consistent with other report [46]. Therefore, we choose the 460 nm LED as the excitation source in the following gas-sensing tests.

Fig. 7(a–c) show the dynamic resistance curves of ZnO/g-C_3N_4 composites to different concentrations of NO_2 ranging from 1 to 7 ppm under 460 nm light excitation. For all sensors, once exposed to NO_2, the resistance increases immediately. When the sensors are removed to the pure air again, the resistance also can recover to near the baseline rapidly. Furthermore, each sensor has complete response and recovery process without poisoning phenomenon occurring. The linear tendency is observed for ZnO/g-C_3N_4 composite based sensors to NO_2 concentration range from 1 to 7 ppm, as shown in Fig. 7d. The slopes of straight line for three sensors exhibit excellent linear tendency (R^2 = 0.9905, 0.9857, and 0.9970, respectively). It can be seen that the sensor based on ZnO/g-C_3N_4-10 wt% exhibits much higher response than ZnO/g-C_3N_4-5 wt% and ZnO/g-C_3N_4-15 wt%. In the system of ZnO/g-C_3N_4 composites, the heterogeneous interfaces between ZnO and g-C_3N_4 exist lots of active sites which can be used for sensing reaction. Furthermore, the heterogeneous interfaces can also separate the photogenerated carriers generated by g-C_3N_4. When the modification amount of g-C_3N_4 is lower, there are no sufficient heterogeneous interfaces to transport and separate the photogenerated carriers produced by g-C_3N_4. However, the excessive modification may lead to a decrease in the amounts of active sites on the surface of ZnO, which results in poor response. Therefore, the sensor device based on ZnO/g-C_3N_4-10 wt % shows the highest response, and the responses are 10.5, 25.0, 34.3, and 44.8, corresponding to 1, 3, 5, and 7 ppm NO_2, respectively.

A histogram of response and recovery time of ZnO/g-C_3N_4-10 wt% in function of NO_2 concentration was shown in Fig. 8a. The response time is 172, 165, 152, and 142 s while the recovery time is 361, 222, 204, and 190 s, corresponding to 1, 3, 5, and 7 ppm NO_2, respectively. Both response and recovery time decrease with the increase of NO_2 concentration, which is due to the fact that a higher gas concentration means a faster rate of gas diffusion, adsorption and desorption to the surface of sensing material. Furthermore, the recovery time is longer than the response time. In the process of adsorption and desorption of test gases, the adsorption/desorption kinetics determine the dynamic characteristics of gas sensors [19]. Therefore, the longer recovery time indicates that NO_2 molecules have strong connection with the surface of ZnO/g-C_3N_4 composites.

Trace NO_2 sensing of ZnO/g-C_3N_4-10 wt% is probed with concentrations of 100 and 500 ppb, as shown in Fig. 8b. The response is 2.3 and 7.5, corresponding to 100 and 500 ppb NO_2, respectively. The resistance of ZnO/g-C_3N_4-10 wt% still can recover to the baseline slowly in 100 ppb NO_2 though the recovery time has been stretched to dozens

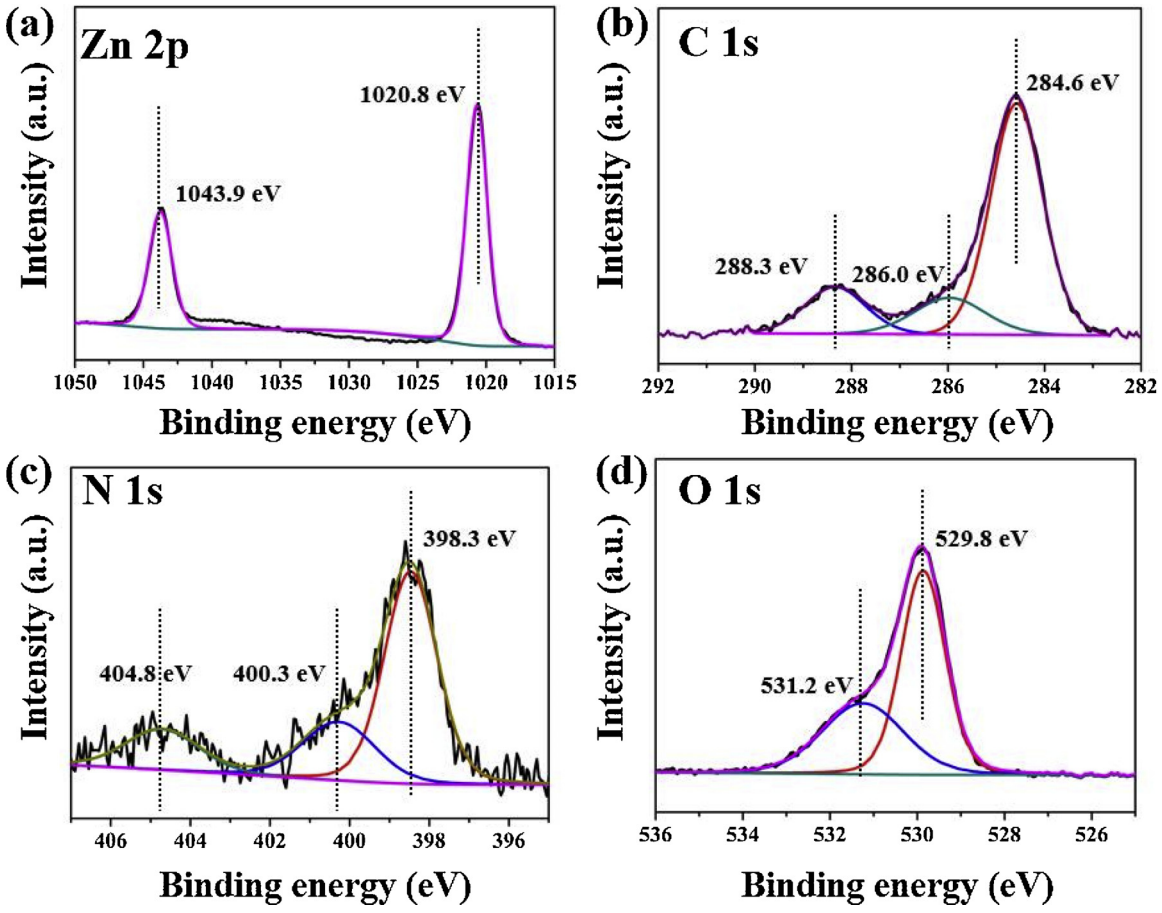

Fig. 5. XPS spectra of ZnO/g-C_3N_4-10 wt%: (a) Zn 2p; (b) C 1s; (c) N 1s; (d) O 1s.

Table 1
Atomic% of different components in ZnO/g-C_3N_4-10 wt% obtained by XPS analysis.

Sample	C%	N%	O%	Zn%
ZnO/g-C_3N_4-10 wt%	54.78	1.96	21.03	22.23

of mins. The excellent response in ppb-level NO_2 proves that ZnO/g-C_3N_4-10 wt% is more sensitive to NO_2 than other samples. Moreover, the signal-to-noise ratio method was acquired to quantify the detection limit (LOD) of NO_2. It should be noted that the LOD is one of the most important indexes reflecting sensitivity and represents the lowest amount of NO_2 in ambient can be detected. The LOD can be calculated by the formula below: [47].

$$\mathrm{LOD} = 3 \times \frac{RMS_{noise}}{K} \quad (1)$$

Where, RMS_{noise} is the root mean square noise and 'K' is the slope value in linear fitting of response (y = 3.03x + 1.88). The sensor noise can be calculated by the relative resistance variation from average resistance measured in ambient. Ten random data were taken to calculate the standard deviation before exposure to NO_2 through the Eq. (2).

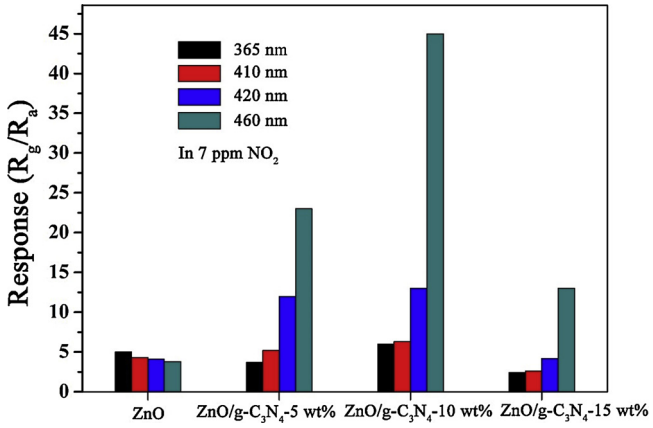

Fig. 6. The responses of as-prepared samples to 7 ppm NO_2 under different wavelength light illumination.

Table 2
Surface area, pore volume and the pore size of pure ZnO and ZnO/g-C_3N_4 composites.

Sample	Pure ZnO	ZnO/g-C_3N_4-5 wt%	ZnO/g-C_3N_4-10 wt%	ZnO/g-C_3N_4-15 wt%
Surface area (m^2/g)	17.807	16.719	16.867	16.470
Pore volume (cm^3/g)	0.0921	0.116	0.115	0.099
Pore size (nm)	31.395	30.375	29.124	35.561

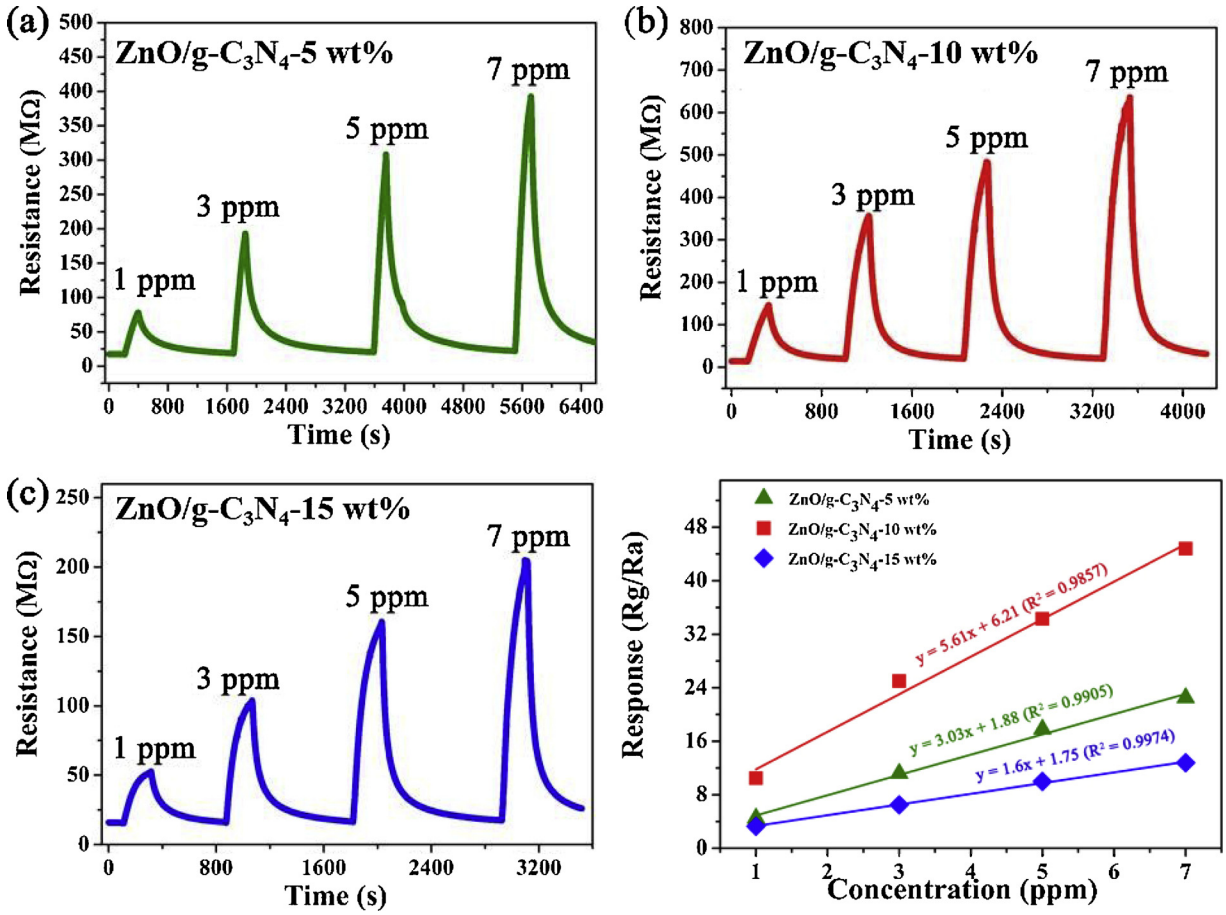

Fig. 7. (a–c) The dynamic resistance curves of ZnO/g-C_3N_4-5 wt%, ZnO/g-C_3N_4-10 wt%, and ZnO/g-C_3N_4-15 wt% to different concentrations of NO_2 under 460 nm light illumination, respectively; (d) linearity of response curves of ZnO/g-C_3N_4 composites.

$$RMS_{noise} = \sqrt{\frac{\sum_{i=1}^{N}(R_i - \overline{R})^2}{N}} \quad (2)$$

Where, R_i is the randomly selected resistance, while $\overline{R}$ is the average resistance of the ten experimental data points. In this work, RMS_{noise} of ZnO/g-C_3N_4-10 wt% is calculated to be 0.0711, and the LOD is 38 ppb.

Fig. 8c shows the repeatability of ZnO/g-C_3N_4-10 wt% to 3 ppm NO_2 in three cycles at room temperature. During three successive injection and extraction process, the resistance of ZnO/g-C_3N_4-10 wt% basically remains unchanged. The responses are 26.0, 26.5, and 26.8, corresponding to the first cycle, second cycle, and the third cycle, respectively, which indicates that ZnO/g-C_3N_4-10 wt% has good repeatability to NO_2. In this work, the selectivity of ZnO/g-C_3N_4-10 wt% was also studied toward different test gases (such as CO, NH_3, C_6H_6, H_2, ethanol, acetone, N_2O and Cl_2), as shown in Fig. 8d. The other gases were tested at a concentration of 100 ppm, and the responses are 1.25 (CO), 1.18 (NH_3), 1.21 (C_6H_6), 1.34 (H_2), 1.42 (ethanol), 1.47 (acetone), 1.50 (N_2O) and 1.43 (Cl_2), respectively, which are all much less than that of NO_2 (44.8 to 7 ppm). The results show that the as-prepared ZnO/g-C_3N_4-10 wt% has better sensitivity and selectivity to NO_2 than other gases.

To investigate the effect of humidity on the response of gas sensors, ZnO/g-C_3N_4-10 wt% was exposed to 3 ppm NO_2 with RH of 50%, 70%, and 90%, respectively. The dynamic resistance curves were shown in Fig. 8e, and the corresponding responses were presented in Fig. 8f. It can be seen that the response decreases as the RH increases from 25% to 90%, which can be attributed to the occupation of adsorption sites on the surface by water vapor. Such influence of humidity in the response of gas sensors was reported in other literatures [35,48]. Significantly, the sensor based on ZnO/g-C_3N_4-10 wt% still maintains complete response and recovery process no matter in low or high humidity, which is meaningful for practical applications. Table 3 shows the sensing performance of NO_2 sensors activated by visible light reported in recent years [17–19,35,49,50]. It can be seen that the ZnO/g-C_3N_4 composite shows great potential in detecting NO_2 at room temperature compared with others.

3.3. Light-assisted NO_2 sensing mechanism

In general, the sensing performance of MOS-based sensors toward test gases is mainly controlled by electrons transfer between the surface of MOS and gas molecules [51,52]. The possible mechanism of light-activated gas sensors has been discussed in other literatures, and it is generally accepted that the photogenerated electron-hole pairs play importance roles in the sensing reaction [53,54].

When ZnO/g-C_3N_4 composite is activated by UV light, photogenerated electron–hole pairs are mainly produced in ZnO. On the one hand, the photogenerated holes can promote the desorption of chemisorbed oxygen species ($O^-_{2(gas)}$) on the surface. On the other hand, oxygen molecules can reattach to the surface again by capturing photogenerated electrons in the CB and form photosorbed oxygen species ($O^-_{2(hv)}$). $O^-_{2(hv)}$ is bound on the surface of ZnO and highly more reactive compared with $O^-_{2(gas)}$ [55]. Once ZnO/g-C_3N_4 composite is exposed to NO_2, the electron depletion layer becomes thicker due to the formation of $NO^-_{2(hv)}$ and $NO^-_{3(hv)}$ by extracting electrons from $O^-_{2(hv)}$ or the remaining photogenerated electrons in the CB, as shown in reaction (3–5).

$$NO_2 + e^-_{hv} \rightarrow NO^-_{2(hv)} \quad (3)$$

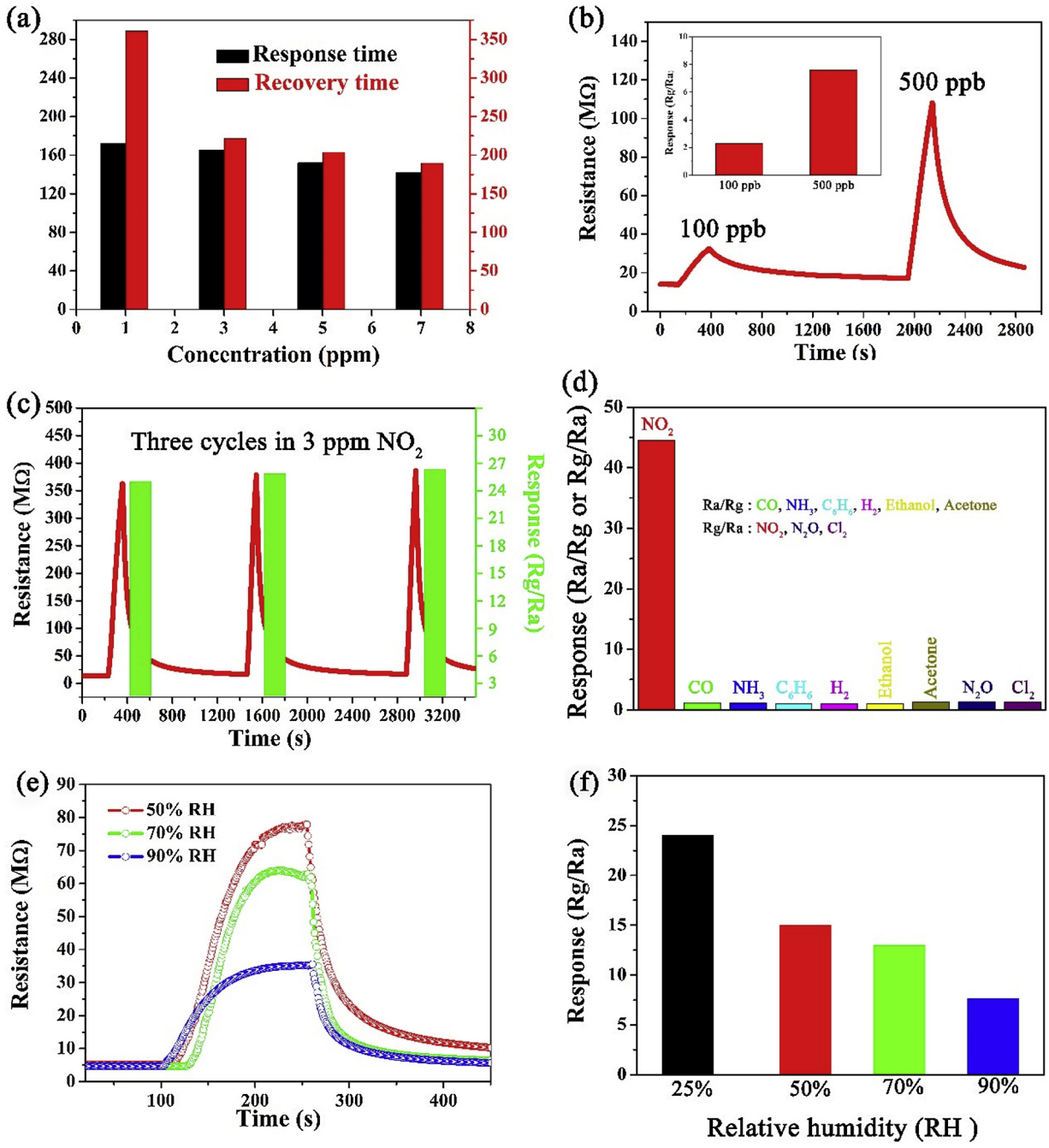

Fig. 8. (a) The histogram of response and recovery time of the ZnO/g-C_3N_4-10 wt% to different concentrations of NO_2; (b) the dynamic resistance curves of the ZnO/g-C_3N_4-10 wt% to 100 and 500 ppb NO_2, and the illustration is the histogram of response; (c) the repeatability of the ZnO/g-C_3N_4-10 wt% to 3 ppm NO_2; (d) the selectivity of the ZnO/g-C_3N_4-10 wt% to various gases; (e–f) the dynamic resistance curves of the ZnO/g-C_3N_4-10 wt% in different relative humidity and the corresponding response.

Table 3
The sensing performance of NO_2 sensors activated by visible light.

Materials	NO_2 (ppm)	Response	T_{res} and T_{rec}	Excitation source	Ref
CdS	5	89%	44 and 113 s	530 nm LED (21 W/m^2)	17
CdSe/ZnO	1	20	3 and > 60 min	535 nm LED (2 W/m^2)	18
Ag/ZnO	5	4.5	140 and ~400 s	460 nm LED (no given)	19
In_2O_3/ZnO	5	54.3	188 and 586 s	460 nm LED (no given)	35
NiO	0.372	31.04%	13.2 and 29.1 min	480 nm LED (no given)	49
WO_3	0.16	2.9	14.9 and 18.3 min	480 nm LED (37 W/m^2)	50
ZnO/g-C_3N_4	7	44.8	140 and 190 s	460 nm LED (12.7 W/m^2)	This work

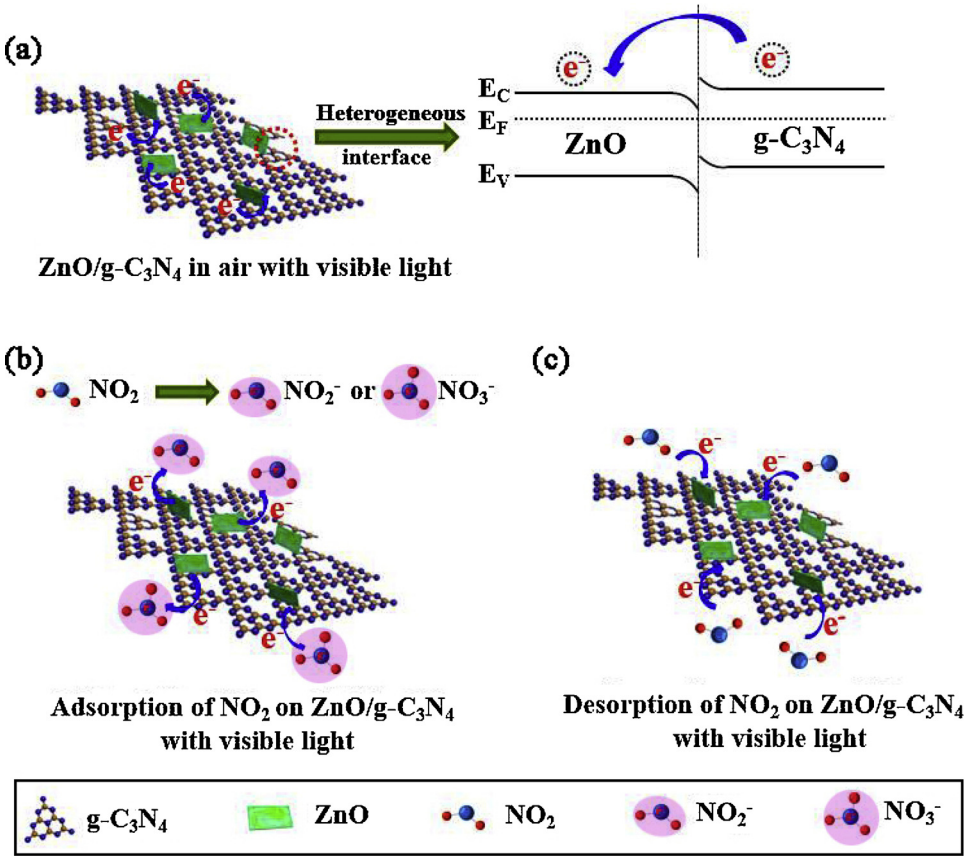

Fig. 9. Schematic illustration of electron transfer process in the sensing reaction.

$$NO_2 + O^-_{2(hv)} \rightarrow NO^-_{2(hv)} + O_{2(gas)} \quad (4)$$

$$2NO_2 + O^-_{2(hv)} + e^-_{hv} \rightarrow 2NO^-_{3(hv)} \quad (5)$$

However, the recombination of photogenerated electron-hole pairs in ZnO seriously restricts the gas-sensing response under UV light [19].

Different from UV light excitation, ZnO cannot absorb the visible light because of its wide bandgap. When ZnO/g-C_3N_4 composites are activated by visible light, only g-C_3N_4 can absorb the visible light to generate photogenerated electron-hole pairs due to its narrow bandgap (2.7 eV). The photogenerated electrons in the CB of g-C_3N_4 will transfer to that of ZnO due to its higher CB, as shown in Fig. 9a. Then, ZnO utilizes the obtained photogenerated electrons for the above gas-sensing reaction. Furthermore, the space transfer of photogenerated electrons from g-C_3N_4 to ZnO greatly promotes the separation of photogenerated electron-hole pairs and prolongs their lifetime [37]. As a result, sufficient photogenerated electrons and holes could be transferred to the surface to participate in the gas-sensing reaction, thus inducing a better response. The schematic illustration of electron transfer processes in the sensing reaction were shown in Fig. 9.

4. Conclusion

In summary, ZnO/g-C_3N_4 composites were synthesized via ultrasonic mixing and subsequent calcination process. The morphology characteristics, phase composition, and their optical properties were characterized by SEM, EDS, XRD, FT-IR, UV–vis, XPS and BET measurements. The SEM results show that ZnO and g-C_3N_4 form the heterojunction successfully. The NO_2 sensing performance of ZnO/g-C_3N_4 composites under various LED light sources with different wavelengths was investigated at room temperature. When under 460 nm light illumination, the ZnO/g-C_3N_4-10 wt% exhibits the highest response of 44.8 to 7 ppm NO_2. The response and recovery time are 142 and 190 s, respectively, and the detection limit is 38 ppb. Furthermore, the ZnO/g-C_3N_4 composite shows excellent selectivity, stability, and certain moisture resistance, which implies the potential application in detecting NO_2.

Declaration of Competing Interest

The authors declare that they have no known competing financial interests or personal relationships that could have appeared to influence the work reported in this paper.

The authors declare the following financial interests/personal relationships which may be considered as potential competing interests:

Acknowledgement

This work was supported by National Nature Science Foundation of China (Nos. 61871198, 61474057 and 61520106003), National key Research and Development Program of China (No. 2016YFC0201002), National High-Tech Research and Development Program of China (863 Program, No. 2014AA06A505).

Appendix A. Supplementary data

Supplementary material related to this article can be found, in the online version, at doi:https://doi.org/10.1016/j.snb.2019.127287.

References

[1] T. Wang, S. Xu, N. Hu, J. Hu, D. Huang, W. Jiang, S. Wang, S. Wu, Y. Zhang, Z. Yang, Microwave preparation and remarkable ethanol sensing properties of ZnO particles with controlled morphologies in water-ethylene glycol binary solvent system, Sens. Actuators B 255 (2018) 1006–1014.
[2] Y. Li, Z. Tao, N. Luo, G. Sun, B. Zhang, H. Jin, H. Bala, J. Cao, Z. Zhang, Y. Wang,

Single-crystalline porous nanoplates-assembled ZnO hierarchical microstructure with superior TEA sensing properties, Sens. Actuators B 290 (2019) 607–615.
[3] R. Yoo, A. Güntner, Y. Park, H. Rim, H. Lee, W. Lee, Sensing of acetone by Al-doped ZnO, Sens. Actuators B 283 (2019) 107–115.
[4] M. Maswanganye, K. Rammutla, T. Mosuang, B. Mwakikung, The effect of Co and in combinational or individual doping on the structural, optical and selective sensing properties of ZnO nanoparticles, Sens. Actuators B 296 (2019) 126655.
[5] Y. Zhou, C. Gao, Y. Guo, UV assisted ultrasensitive trace NO_2 gas sensing based on few-layer MoS_2 nanosheet-ZnO nanowire heterojunctions at room temperature, J. Mater. Chem. A 6 (2018) 10286–10296.
[6] E. Espid, F. Taghipour, Development of highly sensitive ZnO/In_2O_3 composite gas sensor activated by UV-LED, Sens. Actuators B 241 (2017) 828–839.
[7] V. Tomer, S. Duhan, Ordered mesoporous Ag-doped TiO_2/SnO_2 nanocomposite based highly sensitive and selective VOC sensors, J. Mater. Chem. A 4 (2016) 1033–1043.
[8] R. Chen, J. Wang, L. Xiang, Facile synthesis of mesoporous ZnO sheets assembled by small nanoparticles for enhanced NO_2 sensing performance at room temperature, Sens. Actuators B 270 (2018) 207–215.
[9] J. Chavarri, L. Monreal, I. Hurtado, E. Castaño, G. Mandayo, ZnO nanoneedles grown on chip for selective NO_2 detection indoors, Sens. Actuators B 255 (2018) 1244–1253.
[10] C. Liu, H. Tai, P. Zhang, Z. Yuan, X. Du, G. Xie, Y. Jiang, A high-performance flexible gas sensor based on self-assembled PANI-CeO_2 nanocomposite thin film for trace-level NH_3 detection at room temperature, Sens. Actuators B 261 (2018) 587–597.
[11] B. Li, Q. Tian, H. Su, X. Wang, T. Wang, D. Zhang, High sensitivity portable capacitive humidity sensor based on In_2O_3 nanocubes-decorated GO nanosheets and its wearable application in respiration detection, Sens. Actuators B 299 (2019) 126973.
[12] A. Ilin, M. Martyshov, E. Forsh, P. Forsh, M. Rumyantseva, A. Abakumov, A. Gaskov, P. Kashkarov, UV effect on NO_2 sensing properties of nanocrystalline In_2O_3, Sens. Actuators B 231 (2016) 491–496.
[13] T. Hyodo, K. Urata, K. Kamada, T. Ueda, Y. Shimizu, Semiconductor-type SnO_2-based NO_2 sensors operated at room temperature under UV-light irradiation, Sens. Actuators B 253 (2017) 630–640.
[14] J. Hu, C. Zou, Y. Su, M. Li, X. Ye, B. Cai, E. Kong, Z. Yang, Y. Zhang, Light-assisted recovery for a highly-sensitive NO_2 sensor based on RGO-CeO_2 hybrids, Sens. Actuators B 270 (2018) 119–129.
[15] L. Giancaterini, S. Emamjomeh, A. Marcellis, E. Palange, A. Resmini, U. Tamburini, C. Cantalini, The influence of thermal and visible light activation modes on the NO_2 response of WO_3 nanofibers prepared by electrospinning, Sens. Actuators B 229 (2016) 387–395.
[16] T. Yang, K. Gu, M. Zhu, Q. Lu, C. Zhai, Q. Zhao, X. Yang, M. Zhang, ZnO-SnO_2 heterojunction nanobelts: synthesis and ultraviolet light irradiation to improve the triethylamine sensing properties, Sens. Actuators B 279 (2019) 410–417.
[17] H. Li, J. Yoon, C. Lee, K. Lim, J. Yoon, J. Lee, Visible light assisted NO_2 sensing at room temperature by CdS nanoflake array, Sens. Actuators B 255 (2018) 2963–2970.
[18] A. Chizhov, M. Rumyantsev, R. Vasiliev, D. Filatov, K. Drozdov, I. Krylov, A. Abakumov, A. Gaskov, Visible light activated room temperature gas sensors based on nanocrystalline ZnO sensitized with CdSe quantum dots, Sens. Actuators B 205 (2014) 305–312.
[19] Q. Zhang, G. Xie, M. Xu, Y. Su, H. Tai, H. Du, Y. Jiang, Visible light-assisted room temperature gas sensing with ZnO-Ag heterostructure nanoparticles, Sens. Actuators B 259 (2019) 269–281.
[20] Y. Li, Y. Fang, Z. Cao, N. Li, D. Chen, Q. Xu, J. Lu, Construction of g-C_3N_4/PDI@MOF heterojunctions for the highly efficient visible light-driven degradation of pharmaceutical and phenolic micropollutants, Appl. Catal. B-Environ. 250 (2019) 150–162.
[21] R. Wang, X. Kong, W. Zhang, W. Zhu, L. Huang, J. Wang, X. Zhang, X. Liu, N. Hu, Y. Suo, J. Wang, Mechanism insight into rapid photocatalytic disinfection of salmonella based on vanadate QDs-interspersed g-C_3N_4 heterostructures, Appl. Catal. B-Environ. 225 (2018) 228–237.
[22] S. Yang, Y. Gong, J. Zhang, L. Zhan, L. Ma, Z. Fang, R. Vajtai, X. Wang, P. Ajayan, Exfoliated graphitic carbon nitride nanosheets as efficient catalysts for hydrogen evolution under visible light, Adv. Mater. 25 (2013) 2452–2456.
[23] S. Yan, Z. Li, Z. Zou, Photodegradation performance of g-C_3N_4 fabricated by directly heating melamine, Langmuir 25 (2009) 10397–10401.
[24] W. Ong, L. Tan, Y. Ng, S. Yong, S. Chai, Graphitic carbon nitride (g-C_3N_4)-based photocatalysts for artificial photosynthesis and environmental remediation: are we a step closer to achieving sustainability? Chem. Rev. 116 (2016) 7159–7329.
[25] V. Tomer, R. Malik, V. Chaudhary, Y. Mishra, L. Kienle, R. Ahuja, L. Lin, Superior visible light photocatalysis and low-operating temperature VOCs sensor using cubic Ag (0)-MoS_2 loaded g-CN 3D porous hybrid, Appl. Mater. Today 16 (2019) 193–203.
[26] R. Malik, V. Tomer, N. Joshi, T. Dankwort, L. Lin, L. Kienle, Au-TiO_2-loaded cubic g-C_3N_4 nanohybrids for photocatalytic and volatile organic amine sensing applications, ACS Appl. Mater. Inter. 10 (2018) 34087–34097.
[27] R. Malik, V. Tomer, T. Dankwort, Y. Mishra, L. Kienle, Cubic mesoporous Pd-WO_3 loaded graphitic carbon nitride (g-CN) nanohybrids: highly sensitive and temperature dependent VOC sensors, J. Mater. Chem. A 6 (2018) 10718–10730.
[28] N. Joshi, T. Hayasaka, Y. Liu, H. Liu, O. Oliveira Jr, L. Lin, A review on chemiresistive room temperature gas sensors based on metal oxide nanostructures, graphene and 2D transition metal dichalcogenides, Microchim. Acta 185 (2018) 213.
[29] R. Chen, J. Wang, L. Xiang, Facile synthesis of mesoporous ZnO sheets assembled by small nanoparticles for enhanced NO_2 sensing performance at room temperature, Sens. Actuators B 270 (2018) 207–215.
[30] X. Chen, Y. Shen, P. Zhou, X. Zhong, G. Li, C. Han, D. Wei, Li S, Bimetallic Au/Pd nanoparticles decorated ZnO nanowires for NO_2 detection, Sens. Actuators B 289 (2019) 160–168.
[31] S. Liu, B. Yu, H. Zhang, T. Fei, T. Zhang, Enhancing NO_2 gas sensing performances at room temperature based on reduced graphene oxide-ZnO nanoparticles hybrids, Sens. Actuators B 202 (2014) 272–278.
[32] G. Lu, J. Xu, J. Sun, Y. Yu, Y. Zhang, F. Liu, UV-enhanced room temperature NO_2 sensor using ZnO nanorods modified with SnO_2 nanoparticles, Sens. Actuators B 162 (2012) 82–88.
[33] J. Wang, Z. Yang, X. Gao, W. Yao, W. Wei, X. Chen, R. Zong, Y. Zhu, Core-shell g-C_3N_4@ZnO composites as photoanodes with double synergistic effects for enhanced visible-light photoelectrocatalytic activities, Appl. Catal. B-Environ. 217 (2017) 169–180.
[34] J. Wang, Y. Xia, H. Zhao, G. Wang, L. Xiang, J. Xu, S. Komarneni, Oxygen defects-mediated Z-scheme charge separation in g-C_3N_4/ZnO photocatalysts for enhanced visible-light degradation of 4-chlorophenol and hydrogen evolution, Appl. Catal. B-Environ. 217 (2017) 169–180.
[35] J. Park, S. Kim, A. Bard, Novel carbon-doped TiO_2 nanotube arrays with high aspect ratios for efficient solar water splitting, Nano Lett. 6 (2016) 24–28.
[36] S. Guo, X. Li, J. Zhu, T. Tong, B. Wei, Au NPs@MoS_2 sub-micrometer sphere-ZnO nanorod hybrid structures for efficient photocatalytic hydrogen evolution with excellent stability, Small 12 (2016) 5692–5701.
[37] T. Wang, Q. Yu, S. Zhang, X. Kou, P. Sun, G. Lu, Rational design of 3D inverse opal heterogeneous composite microspheres as excellent visible-light-induced NO_2 sensors at room temperature, Nanoscale 10 (2018) 4841–4851.
[38] Y. Zhang, Y. Liu, L. Zhou, D. Liu, F. Liu, F. Liu, X. Liang, X. Yan, Y. Gao, G. Lu, The role of Ce doping in enhancing sensing performance of ZnO-based gas sensor by adjusting the proportion of oxygen species, Sens. Actuators B 273 (2018) 991–998.
[39] H. Yan, H. Yang, TiO_2-g-C_3N_4 composite materials for photocatalytic H_2 evolution under visible light irradiation, Journal Alloy. Comp. 509 (2011) 26–29.
[40] P. He, L. Song, S. Zhang, X. Wu, Q. Wei, Synthesis of g-C_3N_4/Ag_3PO_4 heterojunction with enhanced photocatalytic performance, Mater. Res. Bull. 51 (2014) 432–437.
[41] X. Yuan, S. Duan, G. Wu, L. Sun, G. Cao, D. Li, H. Xu, Q. Li, D. Xi, Enhanced catalytic ozonation performance of highly stabilized mesoporous ZnO doped g-C_3N_4 composite for efficient water decontamination, Appl. Catal. A-Gen. 551 (2018) 129–138.
[42] Y. Park, R. Yoo, S. Park, J. Lee, H. Jung, H. Lee, W. Lee, Highly sensitive and selective isoprene sensing performance of ZnO quantum dots for a breath analyzer, Sens. Actuators B 290 (2019) 258–266.
[43] R. Ma, J. Guo, D. Wang, M. He, S. Xun, J. Gu, W. Zhu, H. Li, Preparation of highly dispersed WO_3/few layer g-C_3N_4 and its enhancement of catalytic oxidative desulfurization activity, Colloids Surf. A 572 (2019) 250–258.
[44] F. Liu, X. Chen, X. Wang, Y. Han, X. Song, J. Tian, X. He, H. Cui, Fabrication of 1D Zn_2SnO_4 nanowire and 2D ZnO nanosheet hybrid hierarchical structures for use in triethylamine gas sensors, Sens. Actuators B 291 (2019) 155–163.
[45] J. Zhang, H. Lu, L. Zhang, D. Leng, Y. Zhang, W. Wang, Y. Gao, H. Lu, J. Gao, G. Zhu, Z. Yang, C. Wang, Metal–organic framework-derived ZnO hollow nanocages functionalized with nanoscale Ag catalysts for enhanced ethanol sensing properties, Sens. Actuators B 291 (2019) 458–469.
[46] X. Geng, C. Zhang, M. Debliquy, Cadmium sulfide activated zinc oxide coatings deposited by liquid plasma spray for room temperature nitrogen dioxide detection under visible light illumination, Ceram. Int. 42 (2016) 4845–4852.
[47] R. Jha, J. D'Costa, N. Sakhuja, N. Bhat, $MoSe_2$ nanoflakes based chemiresistive sensors for ppb-level hydrogen sulfide gas detection, Sens. Actuators B 297 (2019) 126687.
[48] X. Wang, Y. Liu, B. Ding, H. Li, X. Zhu, M. Xia, H. Fu, Influence of the addition of nano-TiO_2 and ZnO on the sensing performance of micro-$ZnSnO_3$ ethanol sensors under UV illumination, Sens. Actuators B 276 (2018) 211–221.
[49] X. Geng, D. Lahem, C. Zhang, C. Li, M. Olivier, M. Debliquy, Visible light enhanced black NiO sensors for ppb-level NO_2 detection at room temperature, Ceram. Int. 45 (2019) 4253–4261.
[50] C. Zhang, A. Boudiba, P. Marco, R. Snyders, M. Olivier, M. Debliquy, Room temperature responses of visible-light illuminated WO_3 sensors to NO_2 in sub-ppm range, Sens. Actuators B 181 (2013) 395–401.
[51] H. Long, A. Trochimczyk, S. Cheng, H. Hu, W. Chi, A. Rao, C. Carraro, T. Shi, Z. Tang, R. Maboudian, Nanowire-assembled hierarchical $ZnCo_2O_4$ microstructure integrated with a low-power microheater for highly sensitive formaldehyde detection, ACS Appl. Mater. Inter. 8 (2016) 31764–31771.
[52] S. Maeng, S. Kim, D. Lee, S. Moon, K. Kim, A. Maiti, SnO_2 nanoslab as NO_2 sensor: identification of the NO_2 sensing mechanism on a SnO_2 surface, ACS Appl. Mater. Inter. 6 (2014) 357–363.
[53] J. Zhai, L. Wang, D. Wang, Y. Lin, D. He, T. Xie, UV-illumination room-temperature gas sensing activity of carbon-doped ZnO microspheres, Sens. Actuators B 161 (2012) 292–297.
[54] Q. Geng, X. Lin, R. Si, X. Chen, W. Dai, X. Fu, X. Wang, The correlation between the ethylene response and its oxidation over TiO_2 under UV irradiation, Sens. Actuators B 174 (2012) 449–457.
[55] D. Haridas, A. Chowdhuri, K. Sreenivas, V. Gupta, Enhanced room temperature response of SnO_2 thin film sensor loaded with Pt catalyst clusters under UV radiation for LPG, Sens. Actuators B 153 (2011) 152–157.

Hongtao Wang received his bachelor's degree in 2015 in chemical engineering and technology from Changchun University of Technology, China. He is currently studying for degree of master at Jilin University. His work is studying photoelectric gas-sensing based on metal oxide nanomaterials.

Jihao Bai received the BS degree in Department of Electronic Science and Technology in 2018. He is currently studying for his M.E Sci degree in College of Electronic Science and Engineering, Jilin University, China.

Meng Dai received the BS degree in Department of Micro-Electronics in 2018. She is currently studying for her M.E Sci degree in College of Electronic Science and Engineering, Jilin University, China.

Kunpeng Liu received the BS degree in Department of Electronic Science and Technology in 2018. He is currently studying for his M.E Sci degree in College of Electronic Science and Engineering, Jilin University, China.

Yueying Liu received the BS degree in Department of Electronic Science and Technology in 2017. She is currently studying for her M.E Sci degree in College of Electronic Science and Engineering, Jilin University, China.

Linsheng Zhou received the BS degree in Department of Electronic Science and Technology in 2017. He is currently studying for his M.E Sci degree in College of Electronic Science and Engineering, Jilin University, China.

Fengmin Liu received the BE degree in Department of Electronic Science and Technology in 2000. She received his Doctor's degree in College of Electronic Science and Engineering at Jilin University in 2005. Now she is a professor in Jilin University, China. Her current research is preparation and application of semiconductor oxide, especial in gas sensor and solar cell.

Fangmeng Liu received his PhD degree in 2017 from College of Electronic Science and Engineering, Jilin University, China. Now he is a lecturer of Jilin University, China. His current research interests include the application of functional materials and development of solid state electrolyte gas sensor and flexible device.

Yuan Gao received her PhD degree from Department of Analytical Chemistry at Jilin University in 2012. Now she is an associate professor in Jilin University, China. Her current research is focus on the preparation and application of graphene and semiconductor oxide, especial in gas sensor and biosensor.

Xu Yan received his M.S degree in 2013 from Nanjing Agricultural University. He joined the group of Prof. Xingguang Su at Jilin University and received his Ph.D. degree in June 2017. Since then, he did postdoctoral work with Prof. Geyu Lu and Prof. Junqiu Liu. Currently, his research interests mainly focus on the development of the functional nanomaterials for chem/bio sensors.

Geyu Lu received the B.Sci. degree in Electronic Sciences in 1985 and the M.Sci. degree in 1988 from Jilin University in China and the Dr.Eng. degree in 1998 from Kyushu University in Japan. Now he is a professor of Jilin University, China. His current research interests include the development of chemical sensors and the application of the function materials.